AIAA Journal
Vol. 48, No. 10, October 2010

# Nonlinear Aeroelastic Study for Folding Wing Structures

Peter J. Attar*
*University of Oklahoma, Norman, Oklahoma 73019*
and
Deman Tang† and Earl H. Dowell‡
*Duke University, Durham, North Carolina 27708-0300*

DOI: 10.2514/1.44868

**A folding wing structure consisting of three components (a fuselage, an inboard wing, and an outboard wing) is modeled computationally using a geometrically nonlinear structural dynamics theory based upon von Kármán strains and a three-dimensional vortex lattice aerodynamic model with an exact tangent flow boundary condition and planar wake assumption. The structural dynamic equations of motion are discretized in space using a discrete Ritz basis derived from finite element analysis and component synthesis. Results from the computational model are compared with those from experiments designed and tested in the Duke University wind tunnel for three folding wing configurations. Stable limit cycle oscillations at flow velocities beyond the linear flutter velocity are measured in wind-tunnel experiments and predicted using the computational model. Overall, the limit cycle oscillation magnitude and dominant response frequency results from theory show good agreement with those measured in the experiment. Qualitatively, both the experimental and theoretical limit cycle oscillation curves for the inboard wing show limited nonlinear stiffening with flow velocity for the range of velocities tested. The theoretical model also predicts that the outboard wing limit cycle oscillation tip displacements for the folding wing configuration with the largest outboard folding angle is significantly higher than the two other configurations. Unlike the inboard wing, for each configuration, the outboard wing theoretical limit cycle oscillation curves do show a trend that is reminiscent of a stiffening nonlinearity.**

## Nomenclature

$\mathbf{A}$ = matrix that contains coefficients for component interface constraint equations
$\mathbf{B}_m^l$, $\bar{\mathbf{B}}_m^{nl}$, $\mathbf{B}_m^{nl}$, $\mathbf{B}_b$ = membrane and bending strain interpolation matrices
$\mathbf{C}$ = linear-elastic plane stress constitutive matrix
$\mathbf{n}$ = normal vector to wing surface
$r$ = radial coordinate vector
$\mathbf{T}$ = transformation matrix between disjoint coordinate vector $\zeta_d$ and the independent coordinate vector $\zeta$
$U_{A-B}$, $U_{B-C}$ = potential energy at interface between components due to torsional springs
$\delta$ = variational operator
$\boldsymbol{\epsilon}$ = vector of Green–Lagrange strain components, $\lfloor \epsilon_{xx}, \epsilon_{yy}, \epsilon_{xy} \rfloor^T$
$\epsilon_{xx}$, $\epsilon_{yy}$, $\epsilon_{xy}$ = Green–Lagrange strain components
$\zeta_r$ = reduced vector of independent coordinates
$\Psi_r$ = matrix that relates physical displacement vector $\mathbf{D}$ to reduced coordinate vector $\zeta_r$

## I. Introduction

EFFORTS to develop morphing air vehicles with multiple mission capabilities have recently been undertaken by several research teams, including NASA's Aircraft Morphing program [1] and the Defense Advanced Research Projects Agency's Morphing Aircraft Structures program [2]. One such morphing wing structure is the folding wing concept. With multiple individually articulated sections, various wing geometries can be achieved in flight, allowing for multirole missions with the same aircraft.

Several parametric studies have been performed to assess the linear aeroelastic characteristics of generic folding wing configurations [3–7]. The effect on aeroelastic stability of such parameters as inboard wing folding angle and hinge stiffness were investigated. Conclusions from these studies included 1) a trend of increasing linear flutter dynamic pressure with increasing inboard wing folding angle, 2) higher sensitivity of linear flutter dynamic pressure with respect to outboard hinge stiffness as compared with the inboard hinge stiffness, and 3) morphing wing actuation energy dependence on center of gravity position, Mach number, and wing sweep.

Lee and Chen [8] studied the effect of hinge free play on the linear flutter and limit cycle oscillation (LCO) of folding wings. They observed that, for folding angles between 0 and 30 deg, LCO occurs even when the flight altitude is above that of the linear flutter boundary. Further increases of the folding wing angle above 30 deg resulted in no LCO. They observed that when LCO did occur, it could occur even for very small values of the free-play parameter ($\pm 0.02°$).

In recent work, Tang and Dowell [9] introduced the concept of using component modal analysis to model, efficiently and accurately, multicomponent folding wing configurations. Their results showed that an increase in inboard wing hinge stiffness lead to improved aeroelastic stability, while an increase in outboard hinge stiffness decreased the linear flutter velocity. They also noted that, for certain values of inboard hinge stiffness, a hump-type linear flutter could occur. Their computational results were also compared with the experiment and, in the experiment, LCO was observed. Good agreement was found between computed and measured linear flutter velocities and frequencies. However, due to the linear nature of the structural and aerodynamic computational models used in this work, the prediction of these limit cycles was not possible.

The work presented in this paper is an extension of that presented in [9] to include nonlinear effects in both the structural and aerodynamic models. Geometric nonlinearity in the structure is modeled using von Kármán strains with the Kirchhoff thin-plate theory, and the resulting nonlinear variational statement is discretized with a

---

Received 10 April 2009; revision received 15 July 2010; accepted for publication 16 July 2010.

*Assistant Professor, Department of Aerospace and Mechanical Engineering, 865 Asp Avenue, Felgar Hall Room 212; peter.attar@ou.edu. Member AIAA.

†Research Scientist, Department of Mechanical Engineering and Material Science, Box 90300, Hudson Hall. Member AIAA.

‡William Holland Hall Professor, Department of Mechanical Engineering and Materials Science, Box 90300, Hudson Hall; also Dean Emeritus, Pratt School of Engineering; dowell@ee.duke.edu. Honorary Fellow AIAA (Corresponding Author).

discrete Ritz basis computed using a combined finite element/component synthesis analysis. The flow is modeled using a vortex lattice potential flow model, which accounts for the nonlinear tangent flow boundary conditions. Postlinear flutter limit cycle results from the computational model are compared with those measured in the experiment for three different outboard wing folding angle configurations.

## II. Folding Wing Configuration

A schematic of the folding wing geometry to be investigated is shown in Fig. 1. The folding wing system consists of three separate components: component A (i.e., fuselage), component B (i.e., inboard wing), and component C (i.e., outboard wing). Components A and B are attached through a hinge that is modeled as a set of torsional springs at several points, $P_j$, with spring stiffness, $K_{Aj}$. Components B and C are also attached through a hinge that is modeled as a set of torsional springs at several points, $S_j$, with torsional spring stiffness, $K_{Bj}$. The hinge model is assumed to have negligible mass compared with the wing structure model. The initial folding angles between components A and B and components B and C are $\theta_b$ and $\theta_c$, respectively. Note that $\theta_b$ and $\theta_c$ are the static equilibrium angles. These depend upon the initial unsprung wing folding angle and the sprung deformation due to wing gravity. In addition to the main coordinate system, $xyz$, two additional local coordinate systems, $\zeta_b\eta_b\xi_b$ and $\zeta_c\eta_c\xi_c$ for components B and C, are used, as shown in Fig. 1.

The relationships between the main coordinate system and the local coordinate systems are expressed as follows:

$$\begin{Bmatrix} x \\ y \\ z \end{Bmatrix}_B = \begin{Bmatrix} l_A \tan\beta_0 \\ l_A \\ 0 \end{Bmatrix} + \begin{bmatrix} 1 & 0 & 0 \\ 0 & \cos\theta_B & -\sin\theta_B \\ 0 & \sin\theta_B & \cos\theta_B \end{bmatrix} \begin{Bmatrix} \zeta \\ \eta \\ \xi \end{Bmatrix}_B$$

$$\begin{Bmatrix} x \\ y \\ z \end{Bmatrix}_C = \begin{Bmatrix} (l_A + l_B\cos\theta_B)\tan\beta_0 \\ l_A + l_B\cos\theta_B \\ l_B\sin\theta_B \end{Bmatrix} + \begin{bmatrix} 1 & 0 & 0 \\ 0 & \cos\theta_C & -\sin\theta_C \\ 0 & \sin\theta_C & \cos\theta_C \end{bmatrix} \begin{Bmatrix} \zeta \\ \eta \\ \xi \end{Bmatrix}_C \tag{1}$$

## III. Structural Equations of Motion

### A. Nonlinear Variational Statement

The statement of virtual work requires that the work done by externally applied loads be equal to the work done by inertial, dissipative, and internal forces for any virtual displacement. For a structure with volume $V$ and surface area $S$, this can be written as

$$\int_V \delta\mathbf{u}^T\mathbf{F}\,\mathrm{d}V + \int_S \delta\mathbf{u}^T\boldsymbol{\Phi}_{\mathrm{tr}}\,\mathrm{d}S = \int_V (\delta\mathbf{u}^T\rho\ddot{\mathbf{u}} + \delta\mathbf{u}^T c\dot{\mathbf{u}} + \delta\boldsymbol{\epsilon}^T\boldsymbol{\sigma})\,\mathrm{d}V \tag{2}$$

where $\mathbf{F}$ and $\boldsymbol{\Phi}_{\mathrm{tr}}$ represent prescribed body forces and surface tractions, $\rho$ is the mass density, and $c$ is a damping parameter. Also, $\delta\mathbf{u}$, $\delta\boldsymbol{\epsilon}$, and $\boldsymbol{\sigma}$ represent the vectors of virtual displacements, the virtual Green–Lagrange strains, and the second Kirchhoff–Piola stresses, respectively.

Here, it will be assumed that the Kirchhoff plate theory applies, and that plate rotations are negligible compared with unity (von Kármán assumption). With these simplifications, the Green–Lagrange strains can be written as

$$\epsilon_{xx} = \hat{u}_x + \tfrac{1}{2}\hat{w}_x^2 - z\hat{w}_{xx} \tag{3}$$

$$\epsilon_{yy} = \hat{v}_y + \tfrac{1}{2}\hat{w}_y^2 - z\hat{w}_{yy} \tag{4}$$

$$\epsilon_{xy} = \hat{u}_y + \hat{v}_x + \hat{w}_x\hat{w}_y - 2z\hat{w}_{xy} \tag{5}$$

where, to the degree of accuracy given by the von Kármán and Kirchhoff assumptions, the $x$, $y$, and $z$ displacements $u$, $v$, and $w$, which make up the vector $\mathbf{u}$ in Eq. (2), are given as

$$u \approx \hat{u} - z\frac{\partial\hat{w}}{\partial x} \tag{6}$$

$$v \approx \hat{v} - z\frac{\partial\hat{w}}{\partial y} \tag{7}$$

$$w \approx \hat{w} \tag{8}$$

The displacement vector $\mathbf{u}$ can now be considered to contain only the midplane displacements $\hat{u}$, $\hat{v}$, and $\hat{w}$.

To be consistent with the Kirchhoff and von Kármán assumptions, it is assumed that the constitutive model is linear, plane stress. Hence,

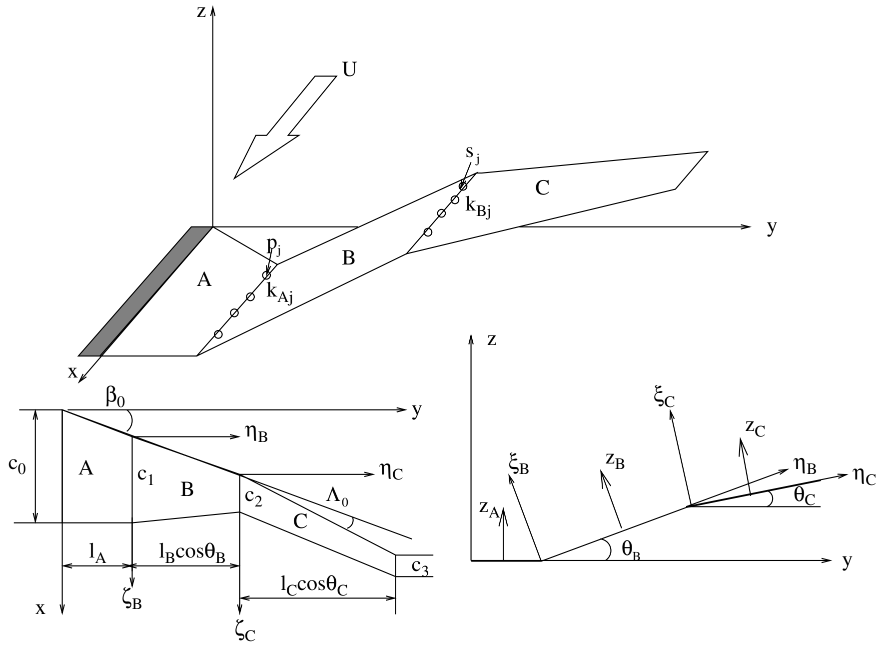

Fig. 1 Schematic of a folding wing geometry and coordinate systems.

given a constant component thickness $h$, we can define the membrane ($\mathbf{N}$) and bending ($\mathbf{M}$) resultant forces as

$$\mathbf{N} = \int_{-h/2}^{h/2} \boldsymbol{\sigma}\, \mathrm{d}z = \int_{-h/2}^{h/2} \mathbf{C}\boldsymbol{\epsilon}\, \mathrm{d}z = \int_{-h/2}^{h/2} \mathbf{C}(\boldsymbol{\epsilon}_m + z\boldsymbol{\chi})\, \mathrm{d}z = h\mathbf{C}\boldsymbol{\epsilon}_m \tag{9}$$

$$\mathbf{M} = \int_{-h/2}^{h/2} \boldsymbol{\sigma} z\, \mathrm{d}z = \int_{-h/2}^{h/2} \mathbf{C}\boldsymbol{\epsilon} z\, \mathrm{d}z = \int_{-h/2}^{h/2} \mathbf{C}(\boldsymbol{\epsilon}_m + z\boldsymbol{\chi}) z\, \mathrm{d}z = \frac{h^3}{12}\mathbf{C}\boldsymbol{\chi} \tag{10}$$

where $\boldsymbol{\sigma} = \mathbf{C}\boldsymbol{\epsilon}$ is the linear plane stress constitutive relation, and $\boldsymbol{\epsilon}_m$ and $\boldsymbol{\chi}$ are the membrane strains and curvatures, respectively [see Eqs. (3–5)].

Integrating the volume integrals in Eq. (2) over the thickness and substituting Eqs. (9) and (10) gives the following virtual work expression:

$$\begin{aligned} h \int_S \delta\mathbf{u}^T \mathbf{F}\, \mathrm{d}S + \int_S \delta\mathbf{u}^T \boldsymbol{\Phi}_{\mathrm{tr}}\, \mathrm{d}S = h \int_S \delta\mathbf{u}^T \rho\ddot{\mathbf{u}}\, \mathrm{d}S \\ + h \int_s \delta\mathbf{u}^T c\dot{\mathbf{u}}\, \mathrm{d}S + \int_S \delta\boldsymbol{\epsilon}_m^T \mathbf{N}\, \mathrm{d}S + \int_S \delta\boldsymbol{\chi}^T \mathbf{M}\, \mathrm{d}S \end{aligned} \tag{11}$$

At this point, a decision must be made as to how Eq. (11) is to be semidiscretized in space. In other words, what sort of trial functions (Ritz basis) will be used to represent the displacements contained in the displacement vector $\mathbf{u}$ and the variation of this vector $\delta\mathbf{u}$. Popular choices include hat functions (in finite element methods) and eigenfunctions of the linearized system. Here, we will choose these functions to be $N$-dimensional vectors derived using component synthesis analysis in combination with finite element analysis (to be more fully explained in the next section).

The displacement vector $\mathbf{D}$ corresponding to the $x$, $y$, and $z$ midplane displacements at $N$ discrete points in space and the variation of this displacement vector $\delta\mathbf{D}$ can now be written, respectively, as

$$\mathbf{D} = \boldsymbol{\Psi}\boldsymbol{\zeta}(t) \tag{12}$$

and

$$\delta\mathbf{D} = \boldsymbol{\Psi}\delta\boldsymbol{\zeta} \tag{13}$$

where $\boldsymbol{\Psi}$ is a $3N \times P$ matrix containing the $P$ $3N$-dimensional basis vectors, and $\boldsymbol{\zeta}$ is a vector of independent generalized time-dependent degrees of freedom. Note if, instead of finite element analysis, continuous functions were used in the component synthesis procedure, $N$ would be equal to one.

Each basis vector in $\boldsymbol{\Psi}$ satisfies the system geometric boundary conditions (in the discrete sense) but not necessarily the natural boundary conditions; hence, these vectors can be considered to be in the admissible class [10].

The vectors of membrane strains and curvatures and virtual membrane strains and curvatures are expressed in terms of the generalized displacements and virtual displacements as (using standard "B matrix" notation [11])

$$\boldsymbol{\epsilon}_m = (\mathbf{B}_m^l + \bar{\mathbf{B}}_m^{nl})\boldsymbol{\zeta} \tag{14}$$

$$\delta\boldsymbol{\epsilon}_m = (\mathbf{B}_m^l + \mathbf{B}_m^{nl})\delta\boldsymbol{\zeta} \tag{15}$$

$$\boldsymbol{\chi} = \mathbf{B}_b\boldsymbol{\zeta} \tag{16}$$

$$\delta\boldsymbol{\chi} = \mathbf{B}_b\delta\boldsymbol{\zeta} \tag{17}$$

Substitution of Eqs. (13–17) into Eq. (11) gives

$$\begin{aligned} \delta\boldsymbol{\zeta}^T\Bigg[ h \int_S \boldsymbol{\Psi}^T \mathbf{F}\, \mathrm{d}S + \int_S \boldsymbol{\Psi}^T \boldsymbol{\Phi}_{\mathrm{tr}}\, \mathrm{d}S - h \int_S \boldsymbol{\Psi}^T \boldsymbol{\Psi}\rho\, \mathrm{d}S\ddot{\boldsymbol{\zeta}} \\ - h \int_S \boldsymbol{\Psi}^T c\boldsymbol{\Psi}\, \mathrm{d}S\dot{\boldsymbol{\zeta}} - \int_S (\mathbf{B}_m^l)^T \mathbf{N}\, \mathrm{d}S - \int_S (\mathbf{B}_m^{nl})^T \mathbf{N}\, \mathrm{d}S \\ - \int_S \mathbf{B}_b^T \mathbf{M}\, \mathrm{d}S \Bigg] = 0 \end{aligned} \tag{18}$$

Considering the arbitrariness of the virtual generalized displacements, Eq. (18) can be written as

$$\begin{aligned} h \int_S \boldsymbol{\Psi}^T \boldsymbol{\Psi}\rho\, \mathrm{d}S\ddot{\boldsymbol{\zeta}} + h \int_S \boldsymbol{\Psi}^T c\boldsymbol{\Psi}\, \mathrm{d}S\dot{\boldsymbol{\zeta}} + \int_S (\mathbf{B}_m^l)^T \mathbf{N}\, \mathrm{d}S \\ + \int_S (\mathbf{B}_m^{nl})^T \mathbf{N}\, \mathrm{d}S + \int_S \mathbf{B}_b^T \mathbf{M}\, \mathrm{d}S = h \int_S \boldsymbol{\Psi}^T \mathbf{F}\, \mathrm{d}S + \int_S \boldsymbol{\Psi}^T \boldsymbol{\Phi}_{\mathrm{tr}}\, \mathrm{d}S \end{aligned} \tag{19}$$

Equation (19) is the semidiscretized (in space) equation of motion for the system. The integrals over $\mathrm{d}S$ in Eq. (19) are performed for each component using the midpoint rule in the local coordinate system of the component. To compute the derivatives needed to construct the B matrices in Eq. (19), third-order finite difference approximations are used.

Discretization in time of Eq. (19) is accomplished through the use of the Hilbert–Hughes–Taylor (HHT) implicit second-order finite difference scheme [11].

### B. Derivation of Ritz Basis Through Component Synthesis

As the details of component modal synthesis are presented in great detail in many references (see [9,10,12–18], the general homogeneous disjoint set of equations for $M$ components will be given without derivation. This set of disjoint equations is generated by writing Lagrange's equations for each of the components and, when put into one matrix system, can be expressed as

$$\mathbf{M}_d\ddot{\boldsymbol{\zeta}}_d + \mathbf{C}_d\dot{\boldsymbol{\zeta}}_d + \mathbf{K}_d\boldsymbol{\zeta}_d = \mathbf{0} \tag{20}$$

where $\boldsymbol{\zeta}_d = [\boldsymbol{\zeta}_1^T, \boldsymbol{\zeta}_2^T, \ldots, \boldsymbol{\zeta}_M^T]$ is the disjoint generalized displacement vector of dimension $R$ and $\mathbf{M}_d$, and $\mathbf{C}_d$ and $\mathbf{K}_d$ are the $R \times R$ block-diagonal disjoint mass and damping and stiffness matrices, respectively. The word disjoint is used here to describe a set of coordinates that are not independent. The value of $R$ corresponds to the sum of the number of basis vectors chosen for each component. After the component (vector) bases are generated using finite element discretization, the disjoint matrices in Eq. (20) are computed using numerical integration (midpoint rule) over each component area (for the in-plane stiffness matrices) and orthonormality (for the out-of-plane stiffness matrices). Inertial contributions are considered for each component of the displacement.

In the current work, the potential energy expressions used to derive Eq. (20) include contributions from the linear plate bending and membrane strain energy and the energy due to the torsional springs at the attachment points. The potential energy $U$ due to these springs, at the interfaces $A - B$ and $B - C$ (see Fig. 1), is given by

$$\begin{cases} U_{A-B} = \frac{1}{2}\sum\limits_j K_{Aj}\left(\left.\frac{\partial\hat{w}_A}{\partial y}\right|_{y=l_A} - \left.\frac{\partial\hat{w}_B}{\partial\eta_B}\right|_{\eta_B=0}\right)^2, & j = 1\cdots N_P \\ U_{B-C} = \frac{1}{2}\sum\limits_j K_{Bj}\left(\left.\frac{\partial\hat{w}_B}{\partial\eta_B}\right|_{\eta_B=l_B} - \left.\frac{\partial\hat{w}_C}{\partial\eta_C}\right|_{\eta_C=0}\right)^2, & j = 1\cdots N_S \end{cases}$$

where $N_P$ and $N_S$ are the total numbers of the attachment points of the two interfaces.

The individual component generalized displacement vectors $\boldsymbol{\zeta}_i$ can in turn be written as

$$\boldsymbol{\zeta}_i^T = [\mathbf{a}_i^T, \mathbf{b}_i^T, \mathbf{q}_i^T] \tag{21}$$

where $\mathbf{a}_i$, $\mathbf{b}_i$, and $\mathbf{b}_i$ are the $i$th component generalized coordinates corresponding to the vectors of $x$, $y$, and $z$ midplane displacements, respectively:

$$\hat{\mathbf{u}}^{i} = \sum_{j} a_{j}^{i} \boldsymbol{\Psi}_{j}^{i} \tag{22}$$

$$\hat{\mathbf{v}}^{i} = \sum_{j} b_{j}^{i} \boldsymbol{\eta}_{j}^{i} \tag{23}$$

$$\hat{\mathbf{w}}^{i} = \sum_{j} q_{j}^{i} \boldsymbol{\gamma}_{j}^{i} \tag{24}$$

In Eqs. (22–24), $\boldsymbol{\psi}_{j}^{i}$, $\boldsymbol{\eta}_{j}^{i}$ and $\boldsymbol{\gamma}_{j}^{i}$ correspond to the $j$th basis vector used to expand the $i$th component $x$, $y$, and $z$ midplane displacement vectors.

In this paper, the $S = 3N_p + 3N_s$ interface constraints are enforced through the writing of a matrix equation of dimension $S \times R$, which is written as

$$\mathbf{A}\,\boldsymbol{\zeta}_d = \mathbf{0} \tag{25}$$

See [10] for a general discussion of the setup of this matrix equation and [9] for the specific constraint equations used here. To remove the redundant coordinates from $\boldsymbol{\zeta}_d$, a coordinate transformation between $\boldsymbol{\zeta}_d$ and the set of independent coordinates $\boldsymbol{\zeta}$ is performed. This transformation is given by the equation

$$\boldsymbol{\zeta}_d = \mathbf{T}\boldsymbol{\zeta} \tag{26}$$

This coordinate transformation consists of finding a basis for the null space of the matrix $\mathbf{A}$ and then expanding $\boldsymbol{\zeta}_d$ in these vectors. The basis is computed using a singular value decomposition of the matrix $\mathbf{A}$. It should be noted that an alternative method of handling the constraints would be through the introduction of Lagrange multipliers into Lagrange's equations [12].

In the previous expression for the disjoint equations of motion, the coordinate transformation between the $3N$ dimensional vector of physical displacements $\mathbf{D}$ and $\boldsymbol{\zeta}_d$ is given by

$$\mathbf{D} = \boldsymbol{\Omega}\boldsymbol{\zeta}_d \tag{27}$$

where $\boldsymbol{\Omega}$ is a matrix composed of all the component basis vectors. Using the coordinate transformation given in Eq. (26), Eq. (27) can be written as

$$\mathbf{D} = \boldsymbol{\Omega}\mathbf{T}\boldsymbol{\zeta} = \boldsymbol{\Psi}\boldsymbol{\zeta} \tag{28}$$

The matrix of global basis vectors $\boldsymbol{\Psi}$ are then used in the nonlinear variational statement [Eq. (19)].

A further reduction in dimension can be performed if Eq. (26) is placed into Eq. (20), and the system is then premultiplied by the transpose of $\mathbf{T}$ [19]. The resulting system can then be cast as an eigenvalue problem and the matrix of eigenstates $\Gamma$ then used in the coordinate transformation:

$$\mathbf{D} = \boldsymbol{\Omega}\mathbf{T}\Gamma\boldsymbol{\zeta}_r = \boldsymbol{\Psi}_r\boldsymbol{\zeta}_r \tag{29}$$

While this procedure can lead to a drastically reduced system dimension, unfortunately the resulting global basis vectors satisfy (in the discrete sense) the linear natural in-plane boundary conditions, which degrades the solution convergence of the nonlinear problem with respect to the required number of basis functions [20].

### C. Component Basis Selection

The components of the folding wing structure studied here have the following material/geometric properties. Component A is constructed from Plexiglas with a modulus of $3.05 \times 10^9$ Pa, a density of 1145 $\mathrm{kg/m^3}$, a Poisson's ratio of 0.45, and a thickness of 0.00238 m. Components B and C are constructed from aluminum with a modulus of $7.2 \times 10^{10}$ Pa, a density of 2850 $\mathrm{kg/m^3}$, a Poisson's ratio of 0.3, and a thickness of 0.000254 m. The stiffness values $K_{Aj}$ and $K_{Bj}$, used for the torsional springs at the component interfaces, are 0.18 $\mathrm{kg \cdot m/s^2}$. For the results presented in this work, the value of $\theta_b$ is 30 deg and three values of $\theta_c$ are investigated: 0, 30 and 60 deg.

The interface constraints [as expressed in Eq. (25)] are that the component midplane deflections $(\hat{u}, \hat{v}, \hat{w})$ in the global $xyz$ coordinate system are to be the same at the hinge attachment points.

Each of the component bases used in this work are computed using a finite element modal analysis. The commercial code ANSYS [21] is used for this purpose. The following types of component bases are used to expand the out-of-plane deflections $\hat{\mathbf{w}}$: 1) the elastic out-of-plane clamped–free–free–free modes from a modal analysis of component A, 2) the out-of-plane elastic and rigid body modes from a free–free–free–free modal analysis of component B, and 3) the out-of-plane elastic and rigid body modes from a free–free–free–free modal analysis of component C.

The component in-plane deflections are expanded using the following types:

1) For component A, both $\hat{\mathbf{u}}$ and $\hat{\mathbf{v}}$ are expanded using the elastic out-of-plane simply supported–free–free–free modes computed with a modal analysis of component A.

2) For component B, both $\hat{\mathbf{u}}$ and $\hat{\mathbf{v}}$ are expanded using the three rigid body modes from a linear plane stress modal analysis of component B and the remaining basis vectors are the elastic out-of-plane free–free–free–free modes for component B.

3) For component C, both $\hat{\mathbf{u}}$ and $\hat{\mathbf{v}}$ are expanded using the three rigid body modes from a linear plane stress modal analysis of component C, and the remaining basis vectors are the elastic out-of-plane free–free–free–free modes.

The number of out-of-plane modes used for components A, B, and C is 25, 75, and 75, respectively, while the number of in-plane modes is 5, 15, and 15. These choices, after the redundant coordinates are eliminated, give a total number of structural degrees of freedom of 221. A convergence study showed that this number of modes gave a good solution convergence.

It should be noted that the choice of the types of bases used in the expansion of the in-plane components is guided by the work presented in [20].

The results for the first five modal frequencies for the three outboard wing folding configurations are shown in Table 1 (denoted as theory in Table 1) along with the corresponding results from an ANSYS modal analysis conducted using a finite element discretization of the complete structure and experiment. Figure 2 shows the first five computed (ANSYS) mode shapes, colored by $z$-displacement contours, for the $\theta_c = 0$ configuration. With the exception of mode 3 for the $\theta_c = 0$ configuration, the comparison between the modal frequencies computed using the current analysis and experiment are favorable. A possible explanation for the differences noted in the third mode of the $\theta_c$ configuration (a difference also present in the ANSYS to experiment comparison) is the following. Additional computations have shown that the third modal frequency is very sensitive to the static configuration. Hence,

**Table 1 Comparison of the first five folding wing modal frequencies**

| | $\theta_c = 0$ | | | $\theta_c = 30$ | | | $\theta_c = 60$ | | |
|---|---|---|---|---|---|---|---|---|---|
| Mode | Present theory | ANSYS | Test | Present theory | ANSYS | Test | Present theory | ANSYS | Test |
| 1 | 4.67 | 4.66 | 4.75 | 4.53 | 4.54 | 4.25 | 4.67 | 4.67 | 4.0 |
| 2 | 16.67 | 16.82 | 16.0 | 17.01 | 17.18 | 17.25 | 16.67 | 16.77 | 15.25 |
| 3 | 22.23 | 22.88 | 32.5 | 36.40 | 37.04 | 31.50 | 22.22 | 22.50 | 23.50 |
| 4 | 41.72 | 42.15 | 43.75 | 43.39 | 43.63 | 46.25 | 41.71 | 41.80 | 47.5 |
| 5 | 66.17 | 67.68 | 75.25 | 67.99 | 69.45 | 73.25 | 66.15 | 67.19 | 75.25 |

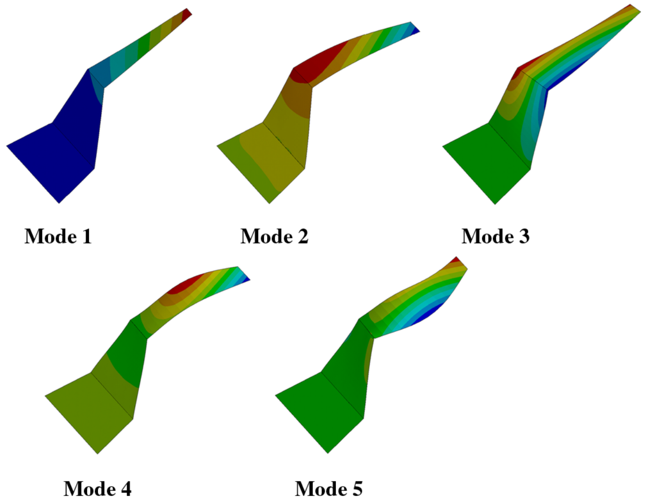
Mode 1 Mode 2 Mode 3

Mode 4 Mode 5

**Fig. 2 First five computed (ANSYS) mode shapes, colored by $z$ displacement contours, for the $\theta_c = 0$ configuration.**

it is possible that this static configuration that, for the computations is assumed to be the nominal position $\theta_b = 30$ and $\theta_c = 0$, is slightly different in the experiment leading to the noted error.

## IV. Aerodynamic Equations

The flowfield about the folding wing model is assumed to be potential flow. Therefore, the equations of motion for the fluid can be reduced to Laplace's equation for the velocity potential $\Phi$:

$$\nabla^2\Phi = 0 \tag{30}$$

The boundary conditions that must be satisfied are those of zero normal flow on the wing; that is,

$$(\nabla\Phi + \mathbf{q}) \cdot \mathbf{n} = 0 \tag{31}$$

and that the disturbance created by the potential must decay at distances far from the wing. The latter equation can be expressed as

$$\lim_{r\to\infty} \nabla\Phi = 0 \tag{32}$$

In Eq. (31), $\mathbf{q}$ is the relative velocity between the undisturbed fluid in the fluid domain and the wing. Using Green's identity, it can be shown [22] that a solution to Eqs. (30–32) can be found by distributing elementary solutions to Laplace's equation on the problem boundaries. For the model presented here, this is accomplished by distributing vortex rings on the wing surface and in the wake.

For most of the computations performed in this work, the small disturbance assumption is not made; hence, the aerodynamic grid used to define bound collocation and vortex locations is moved in three dimensions using the three components of the displacement vector. It was determined through preliminary calculations that imposing the physically correct, but numerically expensive, force-free wake condition had minimal effect on the solution (see Fig. 3). Therefore, with the exception of the data presented in Fig. 3, the results presented here use a planar wake assumption. However, the trailing-edge wake shedding location is taken to be the deformed position. See Katz and Plotkin [23] for further details on the use of vortex rings to discretize the flow model.

The pressure on the wing $p$, which is the external load acting on the structure and used to compute $\mathbf{\Phi}_{\text{tr}}$ in Eq. (19), is calculated using the unsteady (and nonlinear) form of Bernoulli's equation:

$$\frac{p_\infty - p}{\rho_\infty} = \frac{(\nabla\Phi)^2}{2} - \mathbf{q} \cdot \nabla\Phi + \frac{\partial\Phi}{\partial t} \tag{33}$$

where $p_\infty$ and $\rho_\infty$ are the freestream pressure and density, respectively. The time derivative in Eq. (33) is computed using a first-order backward difference approximation.

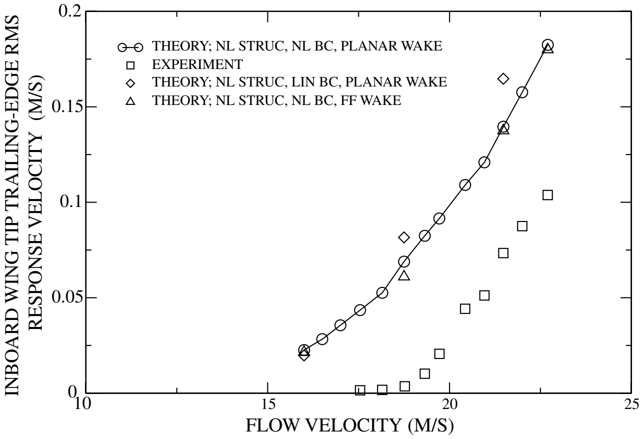

**Fig. 3 Component B trailing-edge tip rms LCO velocity versus flow velocity ($\theta_b = 30$ and $\theta_c = 0$).**

## V. Coupling of Structural and Fluid Models

Coupling of the aerodynamics to the structural dynamics occurs through the specification of the tractions $\mathbf{\Phi}_{\text{tr}}$ in Eq. (19) and by the resulting structural deflection and velocity, which is used in the solution of Eqs. (30) and (31).

Strong coupling of the fluid and structural models is achieved via subiteration within each time step of the simulation [24]. As the grid used in the computation of the component bases is not coincident with the grid used in defining the aerodynamic collocation points, the tractions, structural displacements, and structural velocities are interpolated using local bilinear interpolation [25].

## VI. Theoretical and Experimental Correlations

The results presented in this section are computed using the following numerical parameters. The number of chordwise aerodynamic bound vortex rings is 30, and the number of spanwise bound vortex rings is 33. A total of 114 panels are used in the chordwise direction for the wake. With a time step of 0.0005 s and a minimum flow velocity investigated of 15.00 m/s, this corresponds to a minimum of three chord lengths of wake. Structural damping is not used in the simulation; however, numerical damping is present in the HHT scheme. The damping parameter in the HHT scheme is chosen to be 0.05, which has been found to give good results for nonlinear problems [26,27]. All response results shown in this section are for the structural deflection/velocity in the global $z$-coordinate direction.

Figures 3–5 compare the inboard wing (component B) trailing-edge tip rms velocity of the LCOs from the current computational model to those measured in the wind-tunnel experiments. Results for

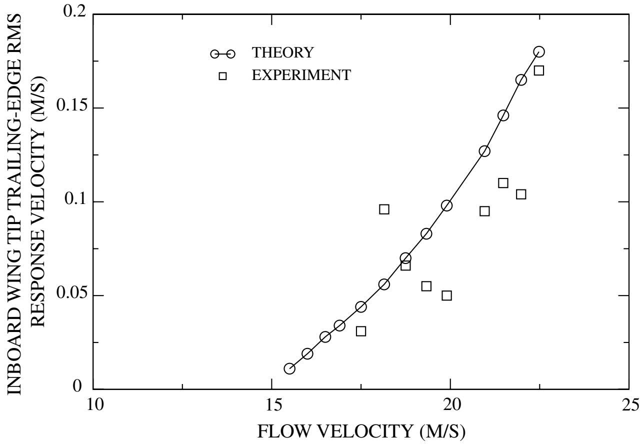

**Fig. 4 Component B trailing-edge tip rms LCO velocity versus flow velocity ($\theta_b = 30$ and $\theta_c = 30$).**

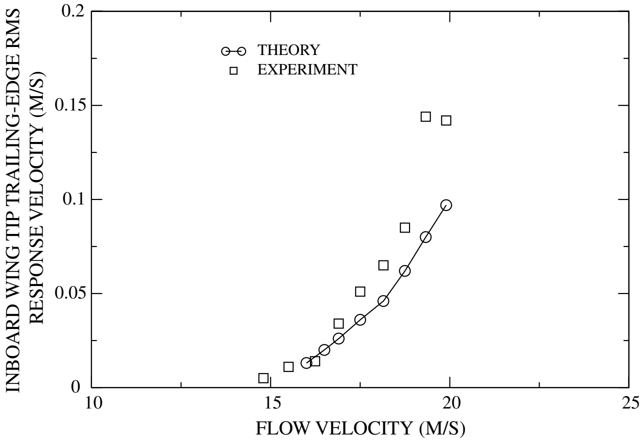

**Fig. 5 Component B trailing-edge tip rms LCO velocity versus flow velocity ($\theta_b = 30$ and $\theta_c = 60$).**

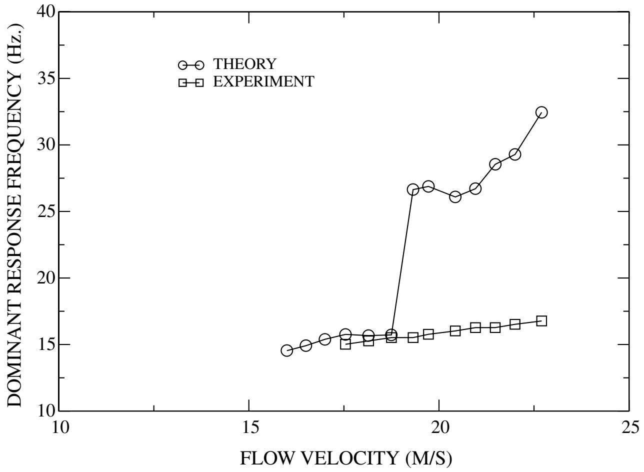

**Fig. 6 LCO dominant response frequency for component B trailing-edge tip velocity versus flow velocity ($\theta_b = 30$ and $\theta_c = 0$).**

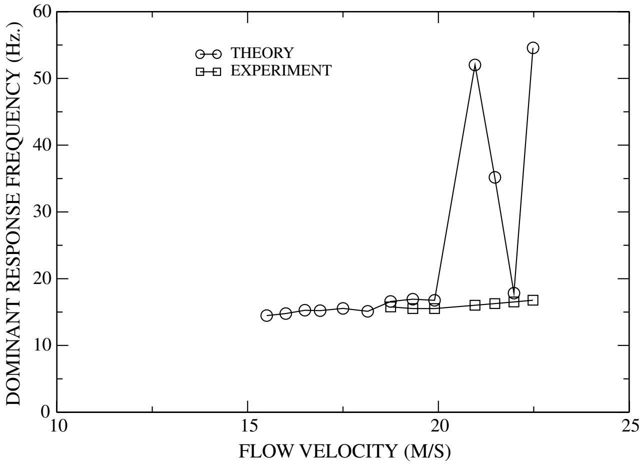

**Fig. 7 LCO dominant response frequency for component B trailing-edge tip velocity versus flow velocity ($\theta_b = 30$ and $\theta_c = 30$).**

three different folding wing configurations are presented. For each of the configurations, the correlation between the computed and measured responses at this point on the folding wing is good. It does appear, however, that the computational model slightly underpredicts the point of bifurcation ("linear flutter velocity"). The computational model predicts linear flutter velocities of 15.5, 15.35, and 15.8 m/s for the configurations corresponding to $\theta_c = 0, 30$, and 60, respectively. While difficult to determine exactly, the linear flutter velocities in the experiment for these configurations are approximately 18, 17.5, and 17 m/s. From Fig. 3, it appears that the largest discrepancy in linear flutter velocity occurs for the $\theta_c = 0$ configuration. As mentioned when discussing Table 1, for this configuration, there is a fairly significant difference between the computed and measured third modal frequency for this configuration. As the flutter mode is dominated by a coupling between modes 2 and 3, a higher mode 3 frequency in the experiment would more than likely result in a higher flutter velocity, as compared with the computation where the mode 3 frequency is lower.

Also shown in Fig. 3 are data that have been computed using the exact nonlinear tangent flow boundary condition and the imposition of the force-wake free condition (denoted as "THEORY: NL STRUC, NL BC, FF WAKE" in the figure), the linearized tangent flow boundary condition and a planar wake (denoted as "THEORY: NL STRUC, LIN BC, PLANAR WAKE" in the figure), and the exact tangent flow boundary condition and a planar wake (denoted as "THEORY: NL STRUC, NL BC, PLANAR WAKE" in the figure). From the results presented in Fig. 3, it is apparent that, for this particular folding wing configuration and set of flow velocities, inclusion of the exact (nonlinear) boundary condition in the model appears to have a slight effect, while the inclusion of the force-free wake model has minimal effect. Results presented in the remainder of this section are computed using a model that includes a nonlinear structural model, the exact nonlinear tangent flow boundary condition, and a planar wake assumption.

A comparison of the theoretical and experimental LCO dominant response frequencies as a function of the flow velocity, as computed from a discrete Fourier transform of the response time history, is shown in Figs. 6–8. For each of the configurations, near the linear flutter velocity, the comparison between the computation and experiment for these response frequencies is good. Also, in both the computation and experiment, the response frequencies appear to increase with increasing flow velocity. However, unlike the experiment, as the flow velocity increases, the computational model results show increasing dynamic complexity in the form of multiple frequencies having significant contributions to the response. This behavior is shown in Fig. 9, which compares the discrete Fourier transform for the computational and experimental models at a flow velocity of 19.7 m/s for the $\theta_c = 0$ configuration. The computational results show the presence of multiple contributing response frequencies, many of which are not integer multiples of each other. This increase in dynamic complexity causes the dominant frequency to switch to a higher frequency for higher flow velocities, as shown in Figs. 6 and 7.

The complex nature of the computational results is further shown in Figs. 10 and 11, which give the velocity response time history and phase plots for the component B tip trailing-edge location at a flow velocity of 22.7 m/s. The folding wing configuration for these two

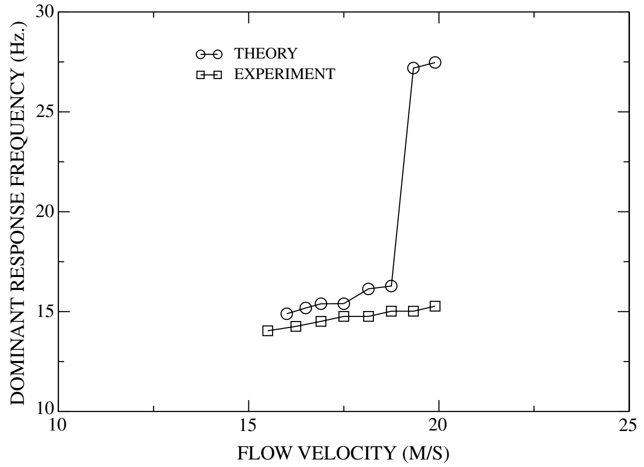

**Fig. 8 LCO dominant response frequency for component B trailing-edge tip velocity versus flow velocity ($\theta_b = 30$ and $\theta_c = 60$).**

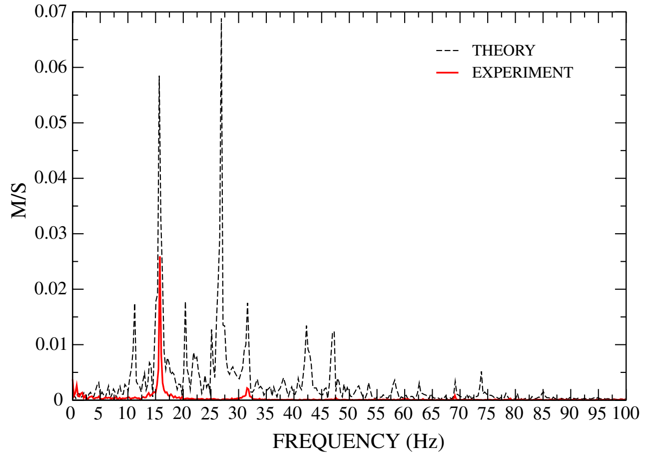

**Fig. 9 Discrete Fourier transform of component B trailing-edge tip LCO velocity at a flow velocity of 19.7 m/s ($\theta_c = 0$).**

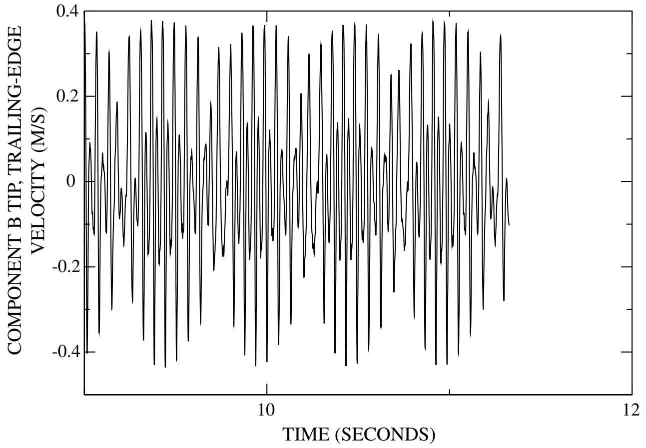

**Fig. 10 Component B trailing-edge tip LCO velocity versus time at a flow velocity of 22.70 m/s ($\theta_c = 0$).**

figures is $\theta_c = 0$. In contrast to Fig. 11, Fig. 12 is a phase plot for the same configuration at a flow velocity of 16 m/s, which is near the linear flutter velocity. The differences in the nature of the phase portraits are apparent.

To attempt to quantify this dynamic complexity, a measure has been used that is computed as the ratio of the magnitude of the maximum Fourier coefficient $A_{\max}$ to the magnitude of all of the Fourier coefficients, where this latter value is computed as

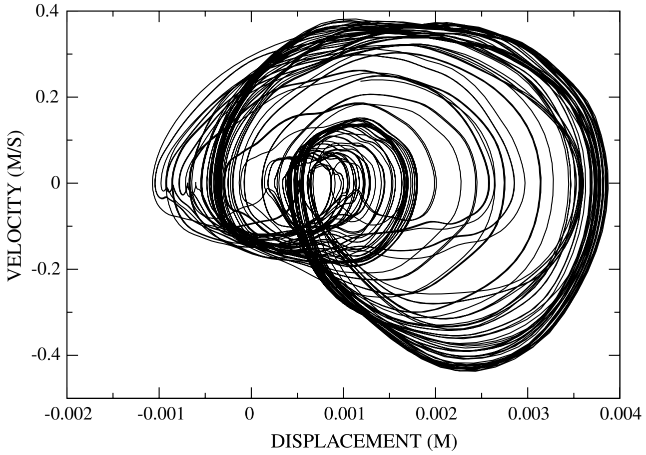

**Fig. 11 Component B trailing-edge tip LCO phase portrait at a flow velocity of 22.70 m/s ($\theta_c = 0$).**

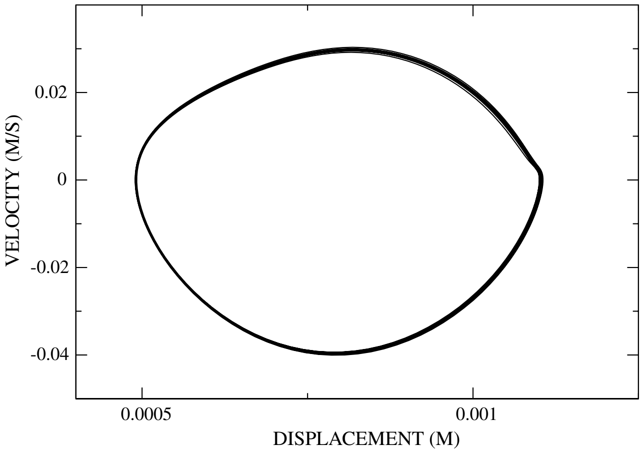

**Fig. 12 Component B phase trailing-edge tip LCO phase portrait at a flow velocity of 16.00 m/s ($\theta_c = 0$).**

$$\sqrt{\sum_i A_i^2}$$

To account for discrete sampling, the maximum and the two surrounding points are used in the computation of $A_{\max}$. A small value of this measure denotes higher dynamic complexity in the form of more frequency components contributing significantly to the response. This measure is plotted versus flow velocity for all three configurations in Figs. 13–15. As can be seen, the computational

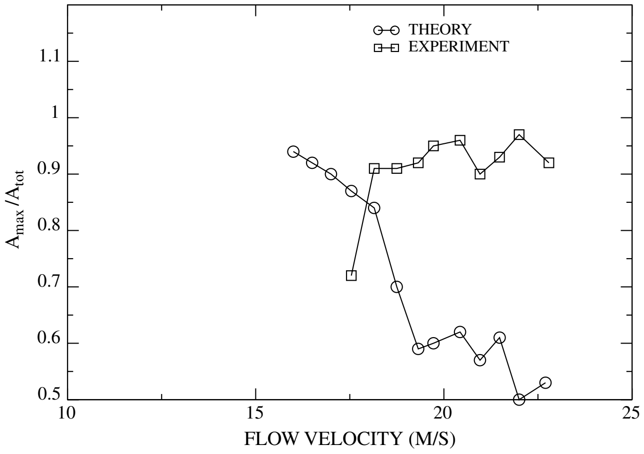

**Fig. 13 Component B tip, trailing-edge velocity dynamic complexity measure versus flow velocity ($\theta_b = 30$ and $\theta_c = 0$).**

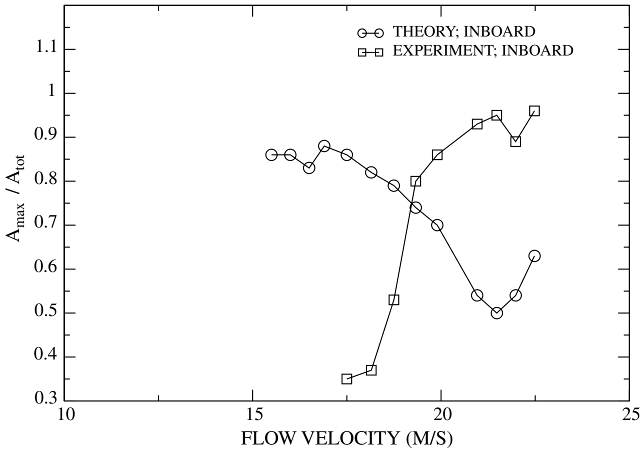

**Fig. 14 Component B tip, trailing-edge velocity dynamic complexity measure versus flow velocity ($\theta_b = 30$ and $\theta_c = 30$).**

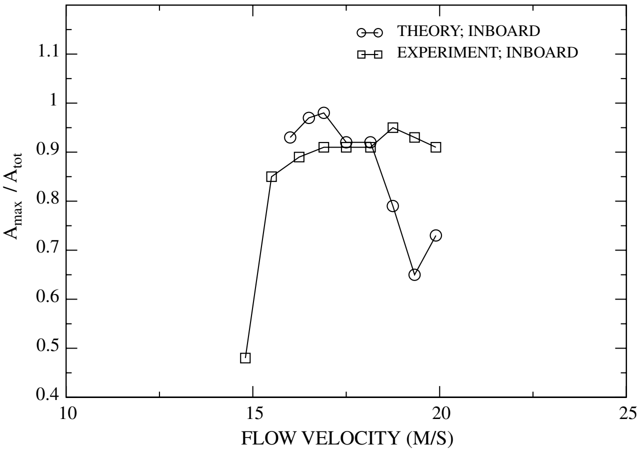

**Fig. 15 Component B tip, trailing-edge velocity dynamic complexity measure versus flow velocity ($\theta_b = 30$ and $\theta_c = 60$).**

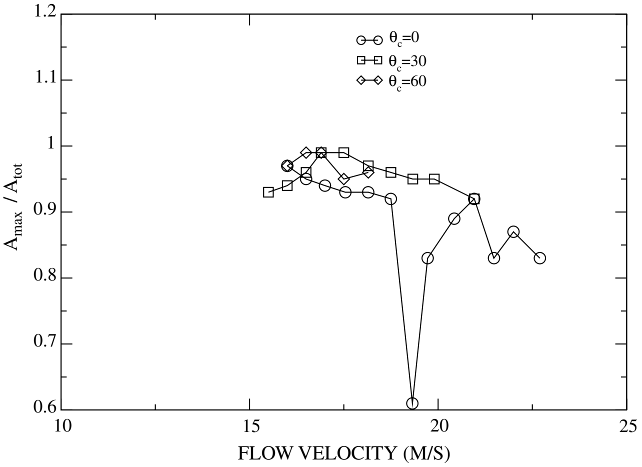

**Fig. 16 Theoretical component C tip, trailing-edge velocity dynamic complexity measure versus flow velocity.**

models clearly show increasing complexity with flow velocity, while the experimental models appear to have a mostly single frequency response. Also, as mentioned when discussing Figs. 6–8, there appears to be a correlation between the dominant response frequency switches and a change in the complexity measure.

It is interesting that the outboard wing computational results shown in Fig. 16 do not show this trend of increasing dynamic complexity with increasing flow velocity. This figure demonstrates that, for the outboard wing, a single frequency response occurs over the flow velocity range investigated. Also from Fig. 17, it is can be noted that the computed tip displacement of the outboard wing is quite large, especially for the two configurations with the smaller outboard wing folding angle ($\theta_c = 0$ and 30). The $\theta_c = 60$ configuration shows much smaller outboard wing tip limit cycle amplitudes and a larger degree of nonlinear stiffening as the flow velocity is increased.

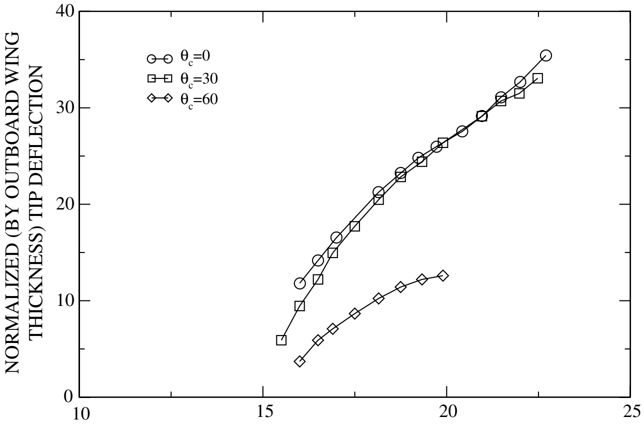

**Fig. 17 Theoretical component C tip, trailing-edge rms LCO displacement versus flow velocity.**

## VII. Conclusions

The nonlinear aeroelastic response characteristics of a three-component (fuselage, inboard wing, and outboard wing) folding wing configuration are investigated both experimentally and theoretically. The theoretical analysis includes a nonlinear structural dynamics model using a discrete Ritz basis derived from finite element and component synthesis analysis and a vortex lattice potential flow model for the fluid.

Computational results for an inboard wing folding angle of 30 deg and three different outboard wing folding angles (0, 30, and 60 deg) are compared with the experiment. For each configuration, LCOs at flow velocities greater than the linear flutter velocity are found in both the experiment and computations. Both the experiment and computation show that differences in the limit cycle behavior do exist between the various folding wing angles.

Overall, the correlation between the computation and the experiment in the postflutter region is good. Predicted and experimental limit cycle response amplitude and dominant frequencies for the inboard wing trailing-edge tip position compare favorably. Through the introduction of a measure of dynamic complexity and inspection of the discrete Fourier transforms, time histories, and phase portraits, it is found that the computational model inboard wing response contains larger contributions from multiple frequencies when compared with the experimental results.

The theoretical model predicts similar outboard limit cycle tip displacements for outboard wing folding angles of 0 and 30 deg, while the configuration where the outboard folding angle is 60 deg shows significantly smaller limit cycle amplitudes and a higher degree of nonlinear stiffening with increasing flow velocity. Experimental and theoretical limit cycle curves for the inboard wing response show limited nonlinear stiffening with flow velocity, while theoretical results for the outboard wing response do show trends that indicate a stiffening effect.

Finally, for the folding wing configuration with an outboard folding angle of 0 deg, investigations into the effect of the aerodynamic tangent flow boundary condition implementation (exact versus linearized) and wake conditions (planar versus force free) were conducted. The results seemed to show that, for the flow velocities examined, including the exact tangent boundary conditions in the aerodynamic model had a small but noticeable effect on the limit cycle characteristics, while including the force-free wake condition had minimal effect.

## Acknowledgments

This work was supported under the U. S. Air Force Office of Scientific Research grant number 313-0016, Nonlinear Aeroelasticity of Novel Configurations, under the direction of John Schmisseur. The first author would like to acknowledge the University of Oklahoma Supercomputing Center, which provided supercomputing time, enabling the completion of this work.

## References

[1] Wlezien, R., Horner, G., McGowan, A., Padula, S., Scott, M., Silcox, R., and Simpson, J., "The Aircraft Morphing Program," AIAA Paper 1998-1927, April 1998.

[2] Wilson, J., "Morphing UAVs Change the Shape of Warfare," *Aerospace America*, Vol. 42, No. 2, Feb. 2004, pp. 28–29.

[3] Dunn, J., Horta, L., Ivanco, T., Piatak, D., Samareh, J., Scott, R., and Wieseman, C., "NASA Contributions to DARPA MAS Program," *Aerospace Flutter and Dynamics Council Meeting*, NASA Langley Research Center, Hampton, VA, May 2004.

[4] Snyder, M., Frank, G., and Sanders, B., "Aeroelastic Analysis of a

Morphing $Z$-Wing Configuration," *Aerospace Flutter and Dynamics Council Meeting*, NASA Langley Research Center, Hampton, VA, May 2004.

[5] Lee, D., and Weisshaar, T., "Aeroelastic Studies on a Folding Wing Configuration," AIAA Paper 2005-1990, April 2005.

[6] Michael, B., and Kamesh, S., "Dynamic Aeroelastic Stability of Morphable Wing Structures," AIAA Paper 2006-2133, 2006.

[7] Snyder, M., Sanders, B., Eastep, F., and Frank, G., "Sensitivity of Flutter to Fold Orientation and Spring Stiffness of a Simple Folding Wing," *Proceedings of the International Forum on Aeroelasticity and Structural Dynamics 2005*, NASA Langley Research Center, Hampton, VA, June–July 2005.

[8] Lee, D., and Chen, P., "Nonlinear Aeroelastic Studies on a Folding Wing Configuration with Free-Play Hinge Nonlinearity," AIAA Paper 2006-1734, 2006.

[9] Tang, D., and Dowell, E. H., "Theoretical and Experimental Aeroelastic Study for Folding Wing Structures," *Journal of Aircraft*, Vol. 45, No. 4, July–Aug. 2008, pp. 1136–1147.
doi:10.2514/1.32754

[10] Meirovitch, L., *Principles and Techniques of Vibrations*, Prentice–Hall, Upper Saddle River, NJ, 1997.

[11] Crisfield, M., *Non-Linear Finite Element Analysis of Solids and Structures*, Vol. 2, Wiley, New York, 1997.

[12] Dowell, E. H., "Free Vibrations of an Arbitrary Structure in Terms of Component Modes," *Journal of Applied Mechanics*, Vol. 39, No. 3, 1972, pp. 727–732.
doi:10.1115/1.3422780

[13] Dowell, E. H., "Component Mode Analysis of a Simple Non-Linear Non-Conservative System," *Journal of Sound and Vibration*, Vol. 80, No. 2, 1982, pp. 233–246.
doi:10.1016/0022-460X(82)90193-6

[14] Dowell, E. H., "Component Modal Analysis of Nonlinear, Nonconservative Systems," *Journal of Applied Mechanics*, Vol. 50, No. 1, 1983, pp. 204–209.
doi:10.1115/1.3166994

[15] Craig, R., *Structural Dynamics: An Introduction to Computer Methods*, Wiley, New York, 1981, Chap. 19.

[16] Castanier, M., Tan, Y., and Pierre, C., "Characteristic Constraint Modes for Component Mode Synthesis," *AIAA Journal*, Vol. 39, No. 6, 2001, pp. 1182–1187.
doi:10.2514/2.1433

[17] Cook, R., Malkus, D., Plesha, M., and Witt, R., *Concepts and Applications of Finite Element Analysis*, 4th ed., Wiley, Hoboken, NJ, 2002.

[18] Wu, S.-C., and Haug, E. J., "Geometric Non-Linear Substructuring for Dynamics of Flexible Mechanical Systems," *International Journal for Numerical Methods in Engineering*, Vol. 26, No. 10, 1988, pp. 2211–2226.
doi:10.1002/nme.1620261006

[19] Dowell, E. H., and Tang, D., *Dynamics of Very High Dimensional Systems*, World Scientific Publ., Hackensack, NJ, 2003.

[20] Attar, P., "Cantilevered Plate Rayleigh–Ritz Trial Function Selection for von Karman's Plate Equations," *Journal of Aircraft*, Vol. 44, No. 2, 2007, pp. 654–661.
doi:10.2514/1.25022

[21] ANSYS User Manual, Ver 11.0, ANSYS, Inc., Canonsburg, PA, 2008.

[22] Ashley, H., and Landahl, M., *Aerodynamics of Wings and Bodies*, Dover, New York, 1965.

[23] Katz, J., and Plotkin, A., *Low-Speed Aerodynamics*, 2nd ed., Univ. Press, Cambridge, MA, 2001.

[24] Attar, P., Dowell, E., and Tang, D., "Modeling Aerodynamic Nonlinearities for Two Aeroelastic Configurations: Delta Wing and Flapping Flag," AIAA Paper 2003-1402, April 2003.

[25] Attar, P., and Gordnier, R., "Aeroelastic Modeling Using a Geometrically Nonlinear $P$-Version Mixed Reissner–Mindlin Plate Element," 48th AIAA Structures, Structural Dynamics, and Materials Conference, AIAA Paper 2007-2318, April 2006.

[26] Hibbitt, H., and Karlsson, B., "Analysis of Pipe Whip," ASME Pressure Vessel and Piping Conference, American Soc. of Mechanical Engineers, Paper 79-PVP-122, Fairfield, NJ, June 1979.

[27] Hibbitt, H., and Karlsson, B., "Analysis of Pipe Whip," Electric Power Res. Inst., TR EPRI NP-1208, Palo Alto, CA, Nov. 1979.

P. Beran
*Associate Editor*